ACS APPLIED MATERIALS & INTERFACES

www.acsami.org

Research Article

Flexible Antireflection Coatings with Enhanced Durability and Antifogging Properties

Uiseok Hwang, Baekmin Q. Kim, Jae-Do Nam,* and Daeyeon Lee*

Cite This: *ACS Appl. Mater. Interfaces* 2024, 16, 10714−10721

Read Online

ACCESS | Metrics & More | Article Recommendations | Supporting Information

ABSTRACT: Antireflection coatings (ARCs) enhance optical clarity and improve light transmission by reducing glare and reflections. The application of conventional ARCs in flexible devices, however, is impeded by their lack of durability, particularly under bending deformation. We develop ARCs that withstand delamination and fracture, remaining intact even after 1000 bending cycles with a 5 cm bending radius. We fabricate integrated ARCs (iARCs) on a poly(methyl methacrylate) (PMMA) substrate by inducing free polymers to infiltrate the interstices of a disordered assembly of hollow silica nanochains and nanospheres. The polydispersity of PMMA creates a refractive index gradient, yielding a broadband antireflection capability. The nanochain-based iARCs are superior to the nanosphere-based coatings in both antireflection properties and mechanical durability, owing to the lower packing density and mechanical interlocking of the nanochains, respectively. Additionally, these nanochain iARCs display antifogging properties stemming from their superhydrophilicity. While our demonstrations are based on PMMA as a model substrate, this methodology is potentially extendable to other polymers, enhancing the iARC's applicability across various practical applications, including flexible and wearable devices.

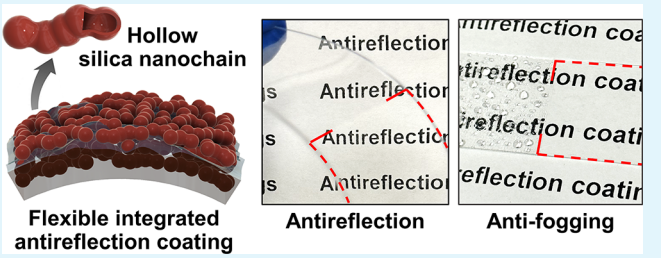

KEYWORDS: *flexible devices, capillary rise, hollow silica nanoparticles, nanocomposites, gradient*

INTRODUCTION

In applications like optical lenses, displays, windows, and solar cells, where high transparency and minimal glare are essential, light reflection due to refractive index contrast between a material and its environment is undesirable. Applying antireflection coatings (ARCs) is a standard method for enhancing light transmittance and reducing surface reflections.[1−4] Considerable progress has been made in improving the properties and functions of ARCs. For example, incorporating nanopores in ARCs lowers their refractive index to below 1.30, yielding high-performance ARCs.[5] Porous ARCs with low refractive indices have been produced by randomly packing silica nanoparticles (NPs) or by incorporating hollow silica NPs in a single-layered monolithic silica coating.[6,7] To achieve broadband antireflection (AR) capabilities, a range of structures including multilayer films, nanopatterned surfaces, graded films, and moth eye-inspired nanostructures have been developed.[8−12]

As portable, wearable, and flexible devices become more prevalent with the desire to reduce the weight and cost of components, glass is increasingly being substituted with transparent polymeric materials such as poly(methyl methacrylate) (PMMA), commonly known as Plexiglas.[13] This shift introduces new complexities in the fabrication and application of ARCs. Although porous silica ARCs offer excellent optical and mechanical properties, their high-temperature fabrication processes (e.g., >300 °C) limit their use on polymeric substrates.[13,14] Several low-temperature, vacuum-based techniques have been developed to deposit low-index porous ARCs on polymer substrates. However, a mismatch in the mechanical properties between the sputter-coated material and the substrate often results in poor adhesion of the ARC to the surface, causing delamination and fracture, particularly under bending deformations.[15,16] Beyond robust surface adhesion, incorporating a refractive index gradient into ARCs could significantly enhance their functionality by effectively suppressing reflections across a broad spectrum of visible light.

In this work, we fabricate ARCs that are physically integrated into polymeric surfaces via capillary rise infiltration (CaRI) of the polymer from the substrate into disordered packings of hollow silica NPs. We evaluate the AR performance and mechanical durability of these integrated ARCs (iARCs) on PMMA substrates (Plexiglas) using both hollow nanospheres and nanochains. The infiltration of the polymer from the substrate into the NP packings drastically enhances

Received: November 30, 2023
Revised: January 20, 2024
Accepted: February 1, 2024
Published: February 20, 2024

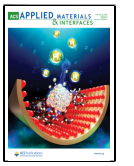

https://doi.org/10.1021/acsami.3c17986
ACS Appl. Mater. Interfaces 2024, 16, 10714−10721

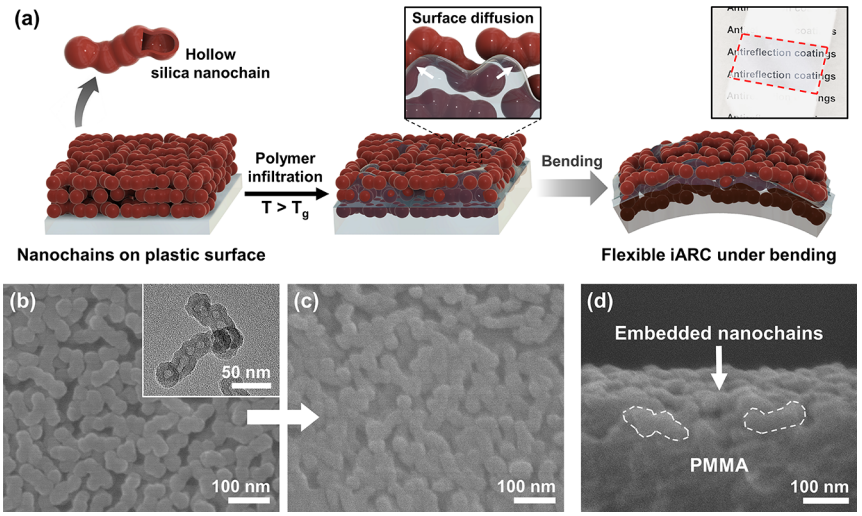

Figure 1. (a) Schematic illustration depicting the CaRI-based fabrication of a graded iARC with hollow silica nanochains on a flexible plastic substrate and iARC under bending deformation; inset digital photo highlights reduced light reflections from the nanochain iARC. Top-down SEM images of (b) neat nanochain film and (c) nanochain iARC for 40 min at 150 °C; inset TEM image shows hollow "peapod"-like structure of the individual nanochains. (d) Cross-sectional SEM image showing the internal structure of the nanochain iARC.

the mechanical durability and adhesion of the iARCs. At the same time, the hollow structure of individual NPs yields coatings with low refractive indices, imparting favorable AR properties. Nanochains outperform nanospheres in both AR and mechanical properties of the resulting iARCs, due to their lower packing density and mechanical interlocking between the nanochains. These nanochain-based iARCs maintain their AR properties even after an abrasion test and more than 1000 mechanical bending cycles, with a bending radius as small as 5 cm; this condition corresponds to a bending strain of 1%, commonly experienced by flexible displays and devices.[17−21] Leveraging the gradient formed during the infiltration of polydisperse polymers into disordered packings of hollow silica nanochains, we fabricate graded iARCs with broadband AR properties across the visible spectrum. These iARCs also exhibit an antifogging capability due to their superhydrophilicity and maintain exceptional mechanical robustness and post-polymer infiltration. Our fabrication approach is adaptable to multiple polymer substrates, broadening the potential use of iARCs in a variety of flexible devices.

RESULTS AND DISCUSSION

We fabricate flexible iARCs with a continuous refractive index gradient by depositing 120 nm-thick layers of disordered hollow silica NPs onto transparent PMMA sheets. This thickness is based on simulation data for the optimal optical thickness of a single-layer ARC for the PMMA substrate (Figure S1). We subsequently induce CaRI of PMMA from the sheets into the interstices of the NP packings at 150 °C which is above the glass transition temperature (T_g) of PMMA (~105 °C), as illustrated in Figure 1a. We use hollow NPs in the form of nanochains and nanospheres. The nanochains have an average thickness of 30 ± 2 nm and an aspect ratio of ~3.8, while the nanospheres have an average diameter of 43 ± 5 nm (see the TEM images in Figure S2). These NPs are synthesized using a modified Stöber method with different concentrations of a silica precursor, tetraethyl orthosilicate (TEOS).[22] The inset photo in Figure 1a (also see Movie S1) vividly demonstrates the efficacy of the nanochain iARC, indicating that the light reflection from the PMMA sheet is significantly suppressed by the iARC, as highlighted by the red dashed line. In a recent report, we demonstrated that infiltrating polymers into disordered assemblies of hollow NPs produces ARCs with high mechanical durability and superb AR performance owing to the dual porosity (i.e., hollow cores of NPs and interparticle voids) in the structure.[22] This study focuses on developing highly flexible ARCs by directly integrating these coatings into polymer substrates.

The internal structure of the nanochain film postpolymer infiltration is characterized by using scanning electron microscopy (SEM). The pristine nanochain film before CaRI exhibits distinct nanochain outlines and interparticle voids (Figure 1b). In contrast, post-CaRI, these voids are partially filled with PMMA, leading to notably less distinct outlines (Figure 1c), although the interparticle voids are not completely filled. The cross-section of the polymer-infiltrated nanochain film reveals that nanochains at the bottom are embedded in the PMMA surface, making them hard to differentiate from the substrate, as shown in Figure 1d. However, the nanochains closer to the top surface are more visibly distinct, confirming a gradient in polymer concentration across the film thickness.

Upon heating at 150 °C, PMMA chains from the substrate infiltrate the interstices of the NP packing via CaRI, immediately generating a continuous gradient throughout the iARC thickness, as confirmed by spectroscopic ellipsometry. The rapid formation of the gradient sharply contrasts with the phenomena observed when monodisperse polymers, such as polystyrene or poly(2-vinylpyridine) are used. In those cases, a dense layer of polymer with a distinct front invades the NP packing, resulting in a clear boundary between polymer-infiltrated and polymer-free NP regions.[23−25] We confirm that a homogeneous nanocomposite film without a gradient is produced when monodisperse PMMA (with a weight-average molecular weight (M_w) of ~350 kg/mol) infiltrates the interstices of a nanochain film, as shown in Figure S3. Consequently, we attribute the instantaneous and spontaneous formation of the refractive index gradient to the polydispersity of PMMA in the commercial sheet. Gel permeation chromatography (GPC) confirms this hypothesis, showing that the polydispersity index (PDI) of PMMA is 3.48 with a

https://doi.org/10.1021/acsami.3c17986
ACS Appl. Mater. Interfaces 2024, 16, 10714−10721

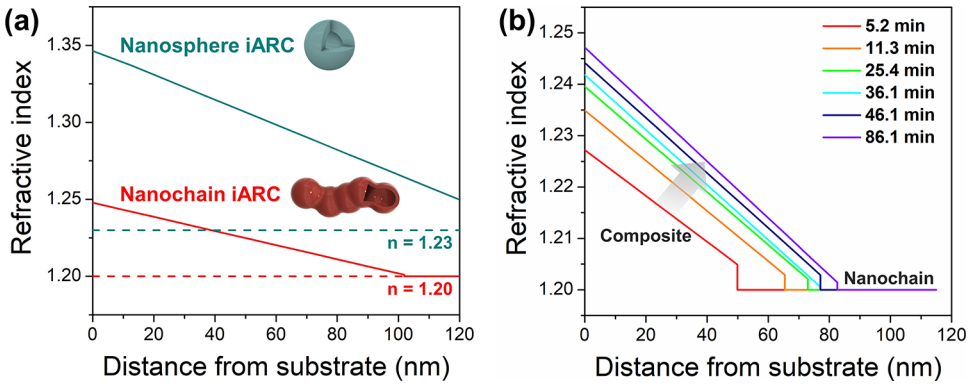

Figure 2. (a) Refractive index profile as a function of distance from substrate for iARCs containing nanochains and nanospheres, annealed for 40 min at 150 °C; dashed lines indicate the refractive indices of corresponding neat NP films. (b) Refractive index profile of PMMA-infiltrated nanochain film at multiple annealing time points, plotted as a function of distance from the substrate.

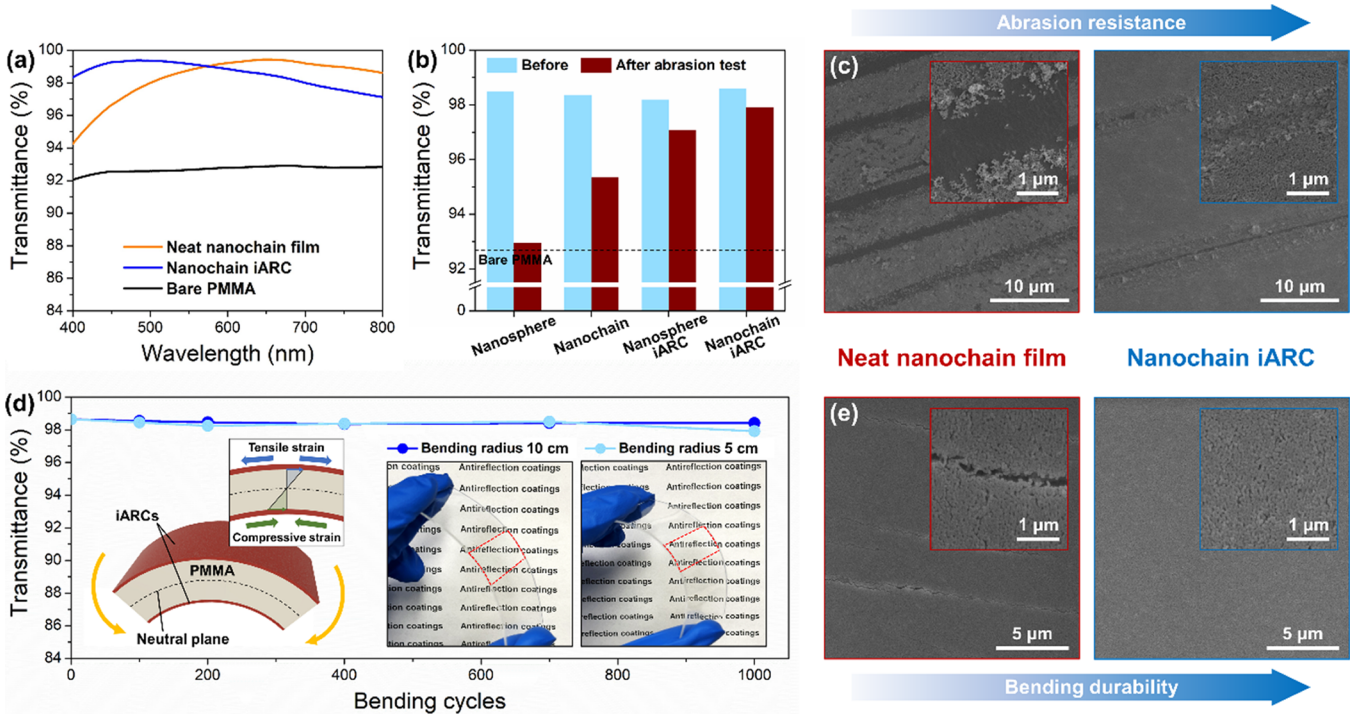

Figure 3. (a) Transmittance spectra of PMMA sheets coated with a neat nanochain film and nanochain iARC. (b) Transmittance of various ARC-coated PMMA sheets before and after abrasion testing and (c) corresponding SEM images showing the surface morphology of neat nanochain film and nanochain iARC post-abrasion test. (d) Average visible light transmittance for nanochain iARC-coated PMMA sheets as a function of the bending cycle for the two bending radii; the inset shows the schematic illustration and digital photos of the iARC-coated PMMA sheets under bending. (e) Corresponding SEM images displaying the surface condition of neat nanochain film and nanochain iARC after undergoing 1000 bending cycles at a bending radius of 5 cm.

number-average molecular weight (M_n) of ~630 kg/mol, as detailed in Figure S4 and Table S1. Our prior studies indicate that the rate of CaRI is heavily influenced by the molecular weight of the polymer.[26,27] Therefore, shorter PMMA chains infiltrate the NP packing more quickly than longer ones, facilitating the rapid and spontaneous formation of a gradient structure.

The refractive index gradient of iARCs incorporating nanochains and nanospheres is characterized using a spectroscopic ellipsometer, as shown in Figure 2a. We employ a graded Cauchy model which consists of ten multilayers with linearly varying refractive indices.[28−31] Both nanochain and nanosphere iARCs display refractive index gradients across their thickness. Specifically, the refractive index of each iARC increases from 1.2 to 1.25 for nanochains and from 1.25 to 1.35 for nanospheres toward the PMMA sheet. This gradient is advantageous for achieving broadband AR properties. The nanochain iARC possesses a refractive index lower than that of its nanosphere counterpart because the refractive index of the neat nanochain film (1.20) is originally lower than that of the neat nanosphere film (1.23). This difference is due to the anisotropic shape of the nanochains, which results in sparser packings compared to nanospheres;[21,32,33] the nanospheres and nanochains generate NP films with uniform refractive indices through the film thickness, indicating the films possess uniform structures. For optimal AR performance, the ideal refractive index range is 1.22−1.23. While the average refractive index of the nanosphere iARC is slightly high at

https://doi.org/10.1021/acsami.3c17986
ACS Appl. Mater. Interfaces 2024, 16, 10714−10721

1.30, the nanochain iARC aligns perfectly with the optimal range, possessing an average refractive index of 1.22.

To monitor how polydisperse PMMA infiltrates into silica NP packings, we track changes in the refractive indices of PMMA-infiltrated nanocomposite and uninfiltrated NP layers, as shown in Figure 2b. During annealing, the nanocomposite layer continues to thicken while maintaining a constant gradient of ~0.5 μm^{-1}. The infiltration process is rapid during the initial 10 min, after which the rate gradually decreases (Figure S5), indicating that the initial stage of infiltration is dominated by short PMMA chains that can move quickly through the NP packings.

We evaluate the transmittance spectra of both neat nanochain film and PMMA-infiltrated nanochain film (nanochain iARC) coated on PMMA sheets, as shown in Figure 3a. The uncoated PMMA sheet shows an average transmittance of ~92.7%. PMMA sheets coated with neat nanochain film and nanochain iARC exhibit increased average transmittances of 98.4 and 98.6%, respectively. The nanochain iARC demonstrates superior broadband AR properties (CV = 0.70%) compared to the neat nanochain film (CV = 1.29%). This enhancement is attributed to the graded structure of the iARC. Following polymer infiltration, there is a noticeable shift in the transmittance band toward the lower wavelength region. Specifically, the peak transmittance bands for the neat nanochain film and nanochain iARC are located at 654 and 467 nm with maxima of 99.7 and 99.6%, respectively. This phenomenon is mainly attributed to the slight decrease in coating thickness by ~15 nm during annealing, as supported by the ellipsometry and simulation results in Figure S6. This reduction is possibly a result of the nanochains becoming more densely packed during CaRI. The simulated transmittance spectra in Figure S6c approximate the experimental data closely; however, there is a slight performance degradation in the experimental results compared with the ideal smooth and monolithic coatings, primarily attributed to light scattering from the rough surfaces of the coatings.

Besides exceptional optical transmittance, mechanical robustness against abrasion and bending is crucial for ARCs in flexible device applications. To assess their mechanical robustness, we conduct abrasion tests on various ARCs. A normal pressure of ~4 kPa (which is equivalent to the pressure generated by stacking 30 smartphones on the surface) is applied via a low-lint wiper placed atop the ARC-coated PMMA sheets. This wiper is slid across the surface, with tests performed on both sides of the sheet. Figure 3b compares the average transmittance for neat NP film and iARC-coated PMMA sheets before and after abrasion testing. The neat nanosphere and nanochain films exhibit significant declines in AR properties post-test, with average transmittance decreasing from 98.5 to 93.0% and from 98.4 to 95.4%, respectively. In contrast, the nanosphere and nanochain iARCs show only minor reductions in transmittance −1.11 to 97.1% and 0.86 to 97.9%, respectively. These results validate that PMMA infiltration significantly enhances the abrasion resistance of these ARCs. This improvement is attributed to robust interfacial adhesion between the NPs and PMMA, as further evidenced by their transmittance spectra in Figure S7. Additionally, the random shape of nanochains confers superior abrasion resistance compared to nanospheres, owing to their propensity to form interlocking structures. In the case of nanospheres, individual particles can be easily displaced under an external force. However, with nanochains, dislodging would require displacing an entire cluster or a network of nanochains, thereby endowing greater abrasion resistance.[32]

After abrasion testing, we examine the surface morphologies of the coatings via SEM, as shown in Figure 3c. For the neat nanochain film, visible scratches aligned with the abrasion direction are evident. NPs are completely dislodged from the substrate, completely exposing the substrate. The nanochain iARC, in contrast, exhibits far fewer and shallower scratches compared to the neat nanochain film. This improvement is attributed to enhanced interfacial adhesion. Notably, most NPs remain embedded in the substrate effectively protecting the PMMA surface after the test, with only the outermost layer of the iARC sustaining slight damage from abrasion; the uppermost region of the nanochain iARC contains relatively smaller amounts of PMMA compared to the bottommost region, and thus can sustain slight damages under abrasion. A similar trend is observed for the nanosphere iARC, as detailed in Figure S8.

Distinct from most conventional ARCs, these iARCs are physically and directly incorporated into the polymeric substrate, resulting in robust adhesion. We believe this configuration, combined with the PMMA chains that bridge nanochains, renders these iARCs particularly well-suited for applications demanding bending resilience. To assess performance deterioration under bending deformation, we subject 1 mm-thick PMMA sheets with nanochain iARCs on both sides to repeated bending cycles. These cycles feature two bending radii of 10 and 5 cm, corresponding to the strains of ~0.5 and ~1%, respectively (Figure 3d) (see Figure S9 for the detailed bending strain calculations). The bending is capped at a radius of ~5 cm because the PMMA sheet itself exhibits intact surface morphology at this bending condition (Figure S10), whereas it cannot withstand a higher bending curvature without breaking. Moreover, coatings that can withstand strains of around ~1% have broad utility in highly flexible applications, including deformable displays, optoelectronics, and energy storage devices.[35] Under the bending strain of ~1%, if the thickness of the PMMA sheet is decreased to 50 μm, the bending radius for the nanochain iARC can be theoretically reduced to 2.5 mm, which is comparable to the bending resistance of commercially available optical films.

Remarkably, the average transmittance remains largely unchanged even after 1000 bending cycles under both conditions; the transmittance of PMMA coated with nanochain iARCs stays nearly constant at 98.0% after 1000 bending cycles with a 5 cm radius, down slightly from an initial 98.6%. In contrast, the neat nanochain film experiences a modest drop of approximately 1%, decreasing from 98.4 to 97.4% after the same number of bending cycles. This transmittance reduction is relatively minor compared to that caused by the abrasion test; however, the repeated application of high tensile strain leads to the formation of microscopic cracks, as seen in Figure 3e. Although the size of these cracks falls below the visible wavelength, minimizing their impact on optical performance,[34] such cracks pose a risk for eventual film delamination from the substrate. In contrast, the nanochain iARC shows no visible cracks or defects even after 1000 bending cycles, suggesting robust bonding between the NPs and between the iARC and the polymeric substrate. This high resistance to fracture and delamination likely arises from the bridging of the nanochains by PMMA chains and the integration of the iARC into the substrate. Typically, there is a trade-off between abrasion resistance and bending resistance, and thus balancing these

https://doi.org/10.1021/acsami.3c17986
ACS Appl. Mater. Interfaces 2024, 16, 10714−10721

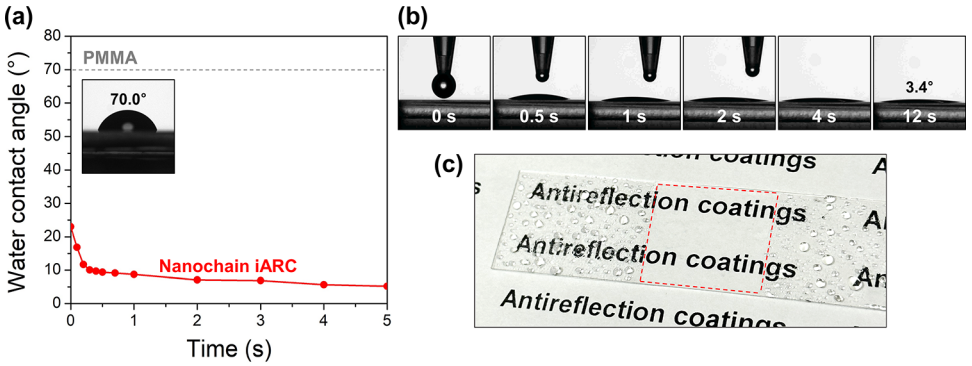

Figure 4. (a) Temporal variation of the water contact angle on a nanochain iARC for a 2 μL water droplet; (b) sequence of digital photos capturing the change in water contact angle over time on the nanochain iARC. (c) Experimental demonstration of antifogging behavior on a nanochain iARC-coated PMMA sheet (red dashed line).

properties in coatings is important for practical applications.[37] Our iARCs, in this respect, meet the criteria with both enhanced antiabrasion properties and a high bending strain of ~1%, which can be applicable to flexible devices.

To provide additional insights into the durability of the iARC, we conduct a peel test on both the neat nanochain film and the nanochain iARC by applying 3 M Scotch tape to the sample surfaces. As shown in Figure S11a, serious damage occurs in the neat nanochain film due to the weak adhesion between the nanochain clusters and the PMMA substrate. Although the nanochain iARC exhibits some deterioration after the peel test, displaying a rough surface, the nanochain clusters still maintain their structures due to the strong interfacial adhesion with the polymer substrate (Figure S11b). The slight damage can be attributed to the detachment of nanochains in the upper part of the iARC with a relatively small amount of bridging polymers.

Fogging, caused by water condensation on plastic surfaces, severely impairs visibility. Therefore, ARCs with antifogging capabilities would enhance their real-world applicability. Prior research indicates that nanoporous silica films achieve complete wetting due to their low contact angles, thereby offering antifogging functionality.[1] To assess the antifogging properties of the nanochain iARC, we conduct time-dependent water contact angle measurements, as shown in Figure 4a,b. A water droplet spreads rapidly on the nanochain iARC surface, falling below 10° within 0.4 s (see Movie S2), confirming the superhydrophilicity of the iARC surface. The observed superhydrophilicity arises from the iARC's graded structure, where the top layer is partially infiltrated with PMMA, leaving the surface both hydrophilic and nanoporous, as corroborated by SEM images and ellipsometry results. Additionally, beyond the inherent superhydrophilicity of the nanochain iARC, the hydrophilicity of the coating can be further enhanced by plasma-treating for 10 s; the water contact angle is reduced from 10° within 0.4 s to 7° within 0.2 s, as shown in Figure S12. The superhydrophilicity of the nanochain iARC contributes to its antifogging capabilities, as shown in Figure 4c. When exposed to a moist environment produced by using a humidifier, condensed water droplets on the iARC spread rapidly on the surface (indicated by the red dashed line). In stark contrast, water droplets condense with a contact angle of 70.0° on bare PMMA, significantly impairing the visibility through the substrate.

Collectively, we precisely tailor the structural and optical properties of the iARCs for PMMA substrates, resulting in excellent combinatorial properties of broadband AR, mechanical, and antifogging properties. Prior reports have theoretically demonstrated that coatings with complex cubic- and quintic-refractive index profiles can exhibit enhanced AR properties compared to the linearly graded coating.[11,38] Such complex structures, however, are difficult to fabricate by using scalable manufacturing methods. The iARCs presented here are easy to fabricate and offer superb broadband AR properties over the entire visible spectrum; moreover, these iARCs are mechanically robust and suppress fogging. The AR properties of the iARC could potentially be further enhanced by creating a complex NP film using combinations of solid NPs and hollow NPs with different shell thicknesses to further engineer the graded structure in the iARCs.[39] Given the versatility of the CaRI process, our methodology can be expanded to various processing conditions and other types of thermoplastic polymer substrates. For example, to prevent heat-induced deformation of the substrate during CaRI, the annealing temperature can be decreased while increasing the annealing time;[23] these adjustments can be applied in conventional industrial heating processes, such as infrared or hot air heating. As alternative transparent plastic substrates for iARCs, materials like polystyrene (PS) (n_{PS} = 1.59; T_g = ~100 °C), polycarbonate (PC) (n_{PC} = 1.58; T_g = ~147 °C), and triacetyl cellulose (TAC) (n_{TAC} = 1.48; T_g = ~200 °C) can be utilized to produce iARCs with optimal refractive indices of ~1.26, ~1.26, and ~1.22, respectively, by adjusting the amount of polymer infiltrated into the NP layer.

CONCLUSIONS

We have developed iARCs on PMMA surfaces that are both mechanically robust and highly flexible. These iARCs are fabricated via CaRI of PMMA into disordered packings of hollow silica nanochains, naturally developing a gradient in their refractive indices due to the polydisperse nature of the polymer of the commercial substrates. The refractive index and gradient of the iARCs can be fine-tuned by adjusting the annealing time and NP shape, optimizing them for superior AR performance. Importantly, the nanochain-based iARCs show significantly enhanced abrasion resistance, which is attributed to strong interfacial bonding with the PMMA substrate and mechanical interlocking among nanochains themselves. Significantly, the nanochain iARCs withstand repeated bending cycles of up to ~1% strain without showing any mechanical degradation. These iARCs also exhibit antifogging properties stemming from their graded structures, expanding their utility

https://doi.org/10.1021/acsami.3c17986
ACS Appl. Mater. Interfaces 2024, 16, 10714−10721

for applications like flexible displays and energy storage devices. Although our current study uses PMMA as a prototype, our methodology is likely transferable to various polymers used in flexible device fabrication.

EXPERIMENTAL SECTION

Materials. Tetraethyl orthosilicate (TEOS, 99%), ammonium hydroxide solution (28 wt %), PMMA (M_w = ∼350,000 g mol^{-1}), and PMMA sheets with a thickness of 1 mm are purchased from Sigma-Aldrich (USA). An aqueous solution of poly(acrylic acid) (PAA) (50 wt %, M_w = ∼5000 g mol^{-1}) is purchased from Polyscience, Inc. (USA).

Synthesis of Hollow Silica Nanochains and Nanospheres. Hollow silica nanochains and nanospheres are synthesized by a modified Stöber method.[22,36] First, PAA (0.35 g) dissolved in ammonium hydroxide solution (17.5 mL) is mixed with ethanol (450 mL), followed by injection of five aliquots of TEOS totaling 7.5 and 12.5 mL, corresponding to the TEOS concentrations of 71.8 and 119.7 mM, respectively, at 1-h intervals under vigorous magnetic stirring at room temperature. After 10 h, a light blue suspension containing silica NPs filled with PAA templates is obtained. The resulting colloids are centrifuged several times with deionized water and ethanol and then redispersed in ethanol. The average thickness and aspect ratio of the nanochains are 30 ± 2 nm and ∼3.8, respectively. The average diameter of the nanospheres is 43 ± 5 nm. The shell thicknesses of hollow nanochains and nanospheres are 10 ± 1 and 14 ± 1 nm, respectively.

Fabrication of iARCs. PMMA sheets are cut into approximately 3 × 3 and 3 × 8 cm^2 rectangles, and both sides of the sheets are oxygen-plasma-treated for 5 s to render the surfaces hydrophilic. Hollow silica NP dispersions (4−8 wt %) are sonicated for 2 h, followed by filtering using syringe filters with a cutoff of 450 nm. Hollow silica NP layers are deposited on both sides of the PMMA substrates via spin-coating (WS-400BZ-6NPP/Lite spin coater, Laurell Technologies Corporation, USA) to form disordered packings of the NPs. The thickness of the NP layer is controlled by changing the rotation speed (3000−10,000 rpm). The prepared samples are thermally annealed in an oven at 150 °C to induce CaRI and yield iARCs.

Characterization. PMMA infiltration into the interparticle voids of the hollow silica NP layer is monitored using spectroscopic ellipsometry (Alpha-SE, J.A. Woollam Co., Inc., USA) while the samples are heated using a heating stage (Linkam THMS 350V, UK) with a temperature resolution of 0.1 °C. The ellipsometry data are collected between λ = 380 and 900 nm at an incident angle of 70° and analyzed using the CompleteEASE software. The ellipsometry data, $\Psi(\lambda)$ and $\Delta(\lambda)$, are modeled using the Cauchy model ($n(\lambda) = A + B/\lambda^2$, $k(\lambda)$=0), where A and B are optical constants, and n and k are the real and imaginary parts of the refractive index, respectively.[22,23,31] All Cauchy modeling is performed with low mean square errors (<15). The thickness and refractive index of the deposited films before and after annealing are also obtained using the ellipsometer.

The size and structure of NPs are examined using a field-emission scanning electron microscope (FE-SEM) (JSM-7500F, JEOL, Japan) and a high-resolution transmission electron microscope (HRTEM) (JEM-F200, JEOL, Japan). The statistical analysis is performed by measuring the size of a minimum of 50 nanoparticles in SEM and TEM images using ImageJ software. The transmittance of the samples is characterized in the range of λ = 400−800 nm using a UV−vis spectrophotometer (Cary 5000, Varian, USA). The surface wettability of coatings is characterized using a time-dependent water contact angle measurement using a goniometer (Biolin Scientific, Attention, Sweden). The molecular weight and polydispersity of PMMA molecules from the commercial PMMA sheets are measured by gel permeation chromatography (GPC) (1260 Infinity, Agilent, USA). The molecular weight calibration curve is obtained using standards with a low polydispersity index (<1.1) and used to determine the molecular weight curve and polydispersity of the PMMA sample.

ASSOCIATED CONTENT

Supporting Information

The Supporting Information is available free of charge at https://pubs.acs.org/doi/10.1021/acsami.3c17986.

Efficacy of the nanochain iARC (MP4)
Water droplet spreading rapidly on the nanochain iARC surface, confirming the superhydrophilicity of the iARC surface (MP4)
Transmittance simulation data, TEM images of hollow silica nanochains and nanospheres synthesized with different TEOS concentrations; in situ spectroscopic ellipsometry data; molecular weight distribution of PMMA molecules consisting of commercial PMMA sheets determined by GPC; transmittance spectra of ARCs after abrasion testing; SEM images of the ARC post-abrasion test; bending strain calculations; SEM images of the PMMA sheet before and after 1000 bending cycles; SEM images of neat nanochain film and nanochain iARC post-peel test; and digital photos of water contact angles on a plasma-treated nanochain iARC (PDF)

AUTHOR INFORMATION

Corresponding Authors

Jae-Do Nam − *Department of Polymer Science and Engineering, Sungkyunkwan University, Suwon 16419, Republic of Korea;* orcid.org/0000-0001-7682-7926; Email: jdnam@skku.edu

Daeyeon Lee − *Department of Chemical and Biomolecular Engineering, School of Engineering and Applied Science, University of Pennsylvania, Philadelphia, Pennsylvania 19104, United States;* orcid.org/0000-0001-6679-290X; Email: daeyeon@seas.upenn.edu

Authors

Uiseok Hwang − *Department of Chemical and Biomolecular Engineering, School of Engineering and Applied Science, University of Pennsylvania, Philadelphia, Pennsylvania 19104, United States; Department of Polymer Science and Engineering, Sungkyunkwan University, Suwon 16419, Republic of Korea*

Baekmin Q. Kim − *Department of Chemical and Biomolecular Engineering, School of Engineering and Applied Science, University of Pennsylvania, Philadelphia, Pennsylvania 19104, United States;* orcid.org/0000-0002-6231-9741

Complete contact information is available at: https://pubs.acs.org/10.1021/acsami.3c17986

Author Contributions

All authors discussed the results, critically revised the manuscript, and gave the final approval.

Notes

The authors declare no competing financial interest.

ACKNOWLEDGMENTS

This work was supported by Penn MRSEC through NSF (NSF DMR 1720530 and DMR 2309043) and NSF CBET-1933704. The authors thank Dr. Jae-Hyun Kim and Dr. Joseph Rosenfeld for helpful discussions and technical support with transmission electron microscopy. U. Hwang acknowledges the support from the Korea Institute for Advancement of

Technology (KIAT) grant funded by the Korean Government (MOTIE) (P0017305, Human Resource Development Program for Industrial Innovation (Global)).

REFERENCES

(1) Lee, D.; Rubner, M. F.; Cohen, R. E. All-Nanoparticle Thin-Film Coatings. *Nano Lett.* **2006**, *6*, 2305−2312.
(2) Gombert, A.; Glaubitt, W.; Rose, K.; Dreibholz, J.; Bläsi, B.; Heinzel, A.; Sporn, D.; Döll, W.; Wittwer, V. Subwavelength-Structured Antireflective Surfaces on Glass. *Thin Solid Films* **1999**, *351*, 73−78.
(3) Du, Y.; Luna, L. E.; Tan, W. S.; Rubner, M. F.; Cohen, R. E. Hollow Silica Nanoparticles in UV−Visible Antireflection Coatings for Poly(methyl methacrylate) Substrates. *ACS Nano* **2010**, *4*, 4308−4316.
(4) Walheim, S.; Schäffer, E.; Mlynek, J.; Steiner, U. Nanophase-Separated Polymer Films as High-Performance Antireflection Coatings. *Science* **1999**, *283*, 520−522.
(5) Zeng, Y.; Song, N.; Lim, S.; Keevers, M.; Wu, Y.; Yang, Z.; Pillai, S.; Jiang, J. Y.; Green, M. Comparative Durability Study of Commercial Inner-Pore Antireflection Coatings and Alternative Dense Coatings. *Sol. Energy Mater. Sol. Cells.* **2023**, *251*, No. 112122.
(6) Zhang, X.; Lan, P.; Lu, Y.; Li, J.; Xu, H.; Zhang, J.; Lee, Y.; Rhee, J. Y.; Choy, K.-L.; Song, W. Multifunctional Antireflection Coatings Based on Novel Hollow Silica−Silica Nanocomposites. *ACS Appl. Mater. Interfaces* **2014**, *6*, 1415−1423.
(7) Zhang, J.; Lan, P.; Li, J.; Xu, H.; Wang, Q.; Zhang, X.; Zheng, L.; Lu, Y.; Dai, N.; Song, W. Sol−Gel Derived Near-UV and Visible Antireflection Coatings from Hybridized Hollow Silica Nanospheres. *J. Sol-Gel Sci. Technol.* **2014**, *71*, 267−275.
(8) Chattopadhyay, S.; Huang, Y. F.; Jen, Y. J.; Ganguly, A.; Chen, K. H.; Chen, L. C. Anti-Reflecting and Photonic Nanostructures. *Mater. Sci. Eng. R Rep.* **2010**, *69*, 1−35.
(9) Yan, X.; Poxson, D. J.; Cho, J.; Welser, R. E.; Sood, A. K.; Kim, J. K.; Schubert, E. F. Enhanced Omnidirectional Photovoltaic Performance of Solar Cells Using Multiple-Discrete-Layer Tailored- and Low-Refractive Index Anti-Reflection Coatings. *Adv. Funct. Mater.* **2013**, *23*, 583−590.
(10) Zhang, X.-X.; Cai, S.; You, D.; Yan, L.-H.; Lv, H.-B.; Yuan, X.-D.; Jiang, B. Template-Free Sol-Gel Preparation of Superhydrophobic ORMOSIL Films for Double-Wavelength Broadband Antireflective Coatings. *Adv. Funct. Mater.* **2013**, *23*, 4361−4365.
(11) Xi, J. Q.; Schubert, M. F.; Kim, J. K.; Schubert, E. F.; Chen, M.; Lin, S.-Y.; Liu, W.; Smart, J. A. Optical Thin-Film Materials with Low Refractive Index for Broadband Elimination of Fresnel Reflection. *Nat. Photonics* **2007**, *1*, 176−179.
(12) Choi, K.; Park, S. H.; Song, Y. M.; Lee, Y. T.; Hwangbo, C. K.; Yang, H.; Lee, H. S. Nano-tailoring the Surface Structure for the Monolithic High-Performance Antireflection Polymer Film. *Adv. Mater.* **2010**, *22*, 3713−3718.
(13) Zahid, M. A.; Cho, Y. H.; Yi, J. Improvement in Optical and Electrical Performance of Hydrophobic and Antireflective Silica Nanoparticles Coating on PMMA for Lightweight PV Module. *Opt. Mater.* **2021**, *119*, No. 111371.
(14) Ai, L.; Zhang, J.; Li, X.; Lu, Y.; Song, W. Universal Low-Temperature Process for Preparation of Multifunctional High-Performance Antireflective Mesoporous Silica Coatings on Transparent Polymeric Substrates. *ACS Appl. Mater. Interfaces* **2018**, *10*, 4993−4999.
(15) Han, Z.; Wang, Z.; Li, B.; Feng, X.; Jiao, Z.; Zhang, J.; Zhao, J.; Niu, S.; Ren, L. Flexible Self-Cleaning Broadband Antireflective Film Inspired by the Transparent Cicada Wings. *ACS Appl. Mater. Interfaces* **2019**, *11*, 17019−17027.
(16) Shu, P.; Ai, L.; Kong, Y.; Ji, H.; Lu, Y.; Zhang, J.; Song, W. UV-Cured Organic−Inorganic Composites for Highly Durable and Flexible Antireflection Coatings. *Appl. Surf. Sci.* **2022**, *584*, No. 152600.
(17) Li, L.; Wang, Y.; Wang, X.; Lin, R.; Luo, X.; Liu, Z.; Zhou, K.; Xiong, S.; Bao, Q.; Chen, G.; et al. Flexible All-Perovskite Tandem Solar Cells Approaching 25% Efficiency with Molecule-Bridged Hole-Selective Contact. *Nat. Energy* **2022**, *7*, 708−717.
(18) Kang, S. B.; Salimzhanov, B.; Park, W. J.; Jeong, M. H.; Kim, J.-Y.; Choi, K. J. Colorful Transparent Silicon Photovoltaics with Unprecedented Flexibility. *Adv. Funct. Mater.* **2022**, *32*, No. 2110435.
(19) Oh, J. M.; Nasir, M.; Ryu, B.; Yun, H. J.; Choi, C.-J.; Bae, J.-S.; Park, H. J. Anomalous Optoelectric Properties of an Ultrathin Ruthenium Film with a Surface Oxide Layer for Flexible Transparent Conducting Electrodes. *Adv. Funct. Mater.* **2022**, *32*, No. 2109330.
(20) Li, Z.; Wu, X.; Li, B.; Zhang, S.; Gao, D.; Liu, Y.; Li, X.; Zhang, N.; Hu, X.; Zhi, C.; et al. Sulfonated Graphene Aerogels Enable Safe-to-Use Flexible Perovskite Solar Modules. *Adv. Energy Mater.* **2022**, *12*, No. 2103236.
(21) Choi, J.; Le, Q. V.; Hong, K.; Moon, C. W.; Han, J. S.; Kwon, K. C.; Cha, P.-R.; Kwon, Y.; Kim, S. Y.; Jang, H. W. Enhanced Endurance Organolead Halide Perovskite Resistive Switching Memories Operable under an Extremely Low Bending Radius. *ACS Appl. Mater. Interfaces* **2017**, *9*, 30764−30771.
(22) Hwang, U.; Nam, J.-D.; Lee, D. Dual Porosity-Enhanced Antireflection Coatings with Continuous Gradient. *ACS Appl. Mater. Interfaces* **2023**, *15*, 40913−40922.
(23) Huang, Y.-R.; Jiang, Y.; Hor, J. L.; Gupta, R.; Zhang, L.; Stebe, K. J.; Feng, G.; Turner, K. T.; Lee, D. Polymer Nanocomposite Films with Extremely High Nanoparticle Loadings via Capillary Rise Infiltration (CaRI). *Nanoscale* **2015**, *7*, 798−805.
(24) Qiang, Y.; Turner, K. T.; Lee, D. Role of Polymer−Nanoparticle Interactions on the Fracture Toughness of Polymer-Infiltrated Nanoparticle Films. *Macromolecules* **2023**, *56*, 122−135.
(25) Kim, B. Q.; Füredi, M.; Venkatesh, R. B.; Guldin, S.; Lee, D. Water-Induced Separation of Polymers from High Nanoparticle-Content Nanocomposite Films. *Small* **2023**, *19*, No. 2302676.
(26) Hor, J. L.; Wang, H.; Fakhraai, Z.; Lee, D. Effects of Polymer−Nanoparticle Interactions on the Viscosity of Unentangled Polymers under Extreme Nanoconfinement during Capillary Rise Infiltration. *Soft Matter* **2018**, *14*, 2438−2446.
(27) Venkatesh, R. B.; Manohar, N.; Qiang, Y.; Wang, H.; Tran, H. H.; Kim, B. Q.; Neuman, A.; Ren, T.; Fakhraai, Z.; Riggleman, R. A.; et al. Polymer-Infiltrated Nanoparticle Films Using Capillarity-Based Techniques: Toward Multifunctional Coatings and Membranes. *Annu. Rev. Chem. Biomol. Eng.* **2021**, *12*, 411−437.
(28) Ogieglo, W.; Wormeester, H.; Wessling, M.; Benes, N. E. Spectroscopic Ellipsometry Analysis of a Thin Film Composite Membrane Consisting of Polysulfone on a Porous α-Alumina Support. *ACS Appl. Mater. Interfaces* **2012**, *4*, 935−943.
(29) Li, D.; Carette, M.; Granier, A.; Landesman, J. P.; Goullet, A. In Situ Spectroscopic Ellipsometry Study of TiO_2 Films Deposited by Plasma Enhanced Chemical Vapour Deposition. *Appl. Surf. Sci.* **2013**, *283*, 234−239.
(30) Ogieglo, W.; Wormeester, H.; Wessling, M.; Benes, N. E. Temperature-Induced Transition of the Diffusion Mechanism of n-Hexane in Ultra-Thin Polystyrene Films, Resolved by In-Situ Spectroscopic Ellipsometry. *Polymer* **2013**, *54*, 341−348.
(31) Kim, B. Q.; Qiang, Y.; Turner, K. T.; Choi, S. Q.; Lee, D. Heterostructured Polymer-Infiltrated Nanoparticle Films with Cavities via Capillary Rise Infiltration. *Adv. Mater. Interfaces* **2021**, *8*, No. 2001421.
(32) Zhang, L.; Feng, G.; Zeravcic, Z.; Brugarolas, T.; Liu, A. J.; Lee, D. Using Shape Anisotropy to Toughen Disordered Nanoparticle Assemblies. *ACS Nano* **2013**, *7*, 8043−8050.
(33) Buskens, P.; Burghoorn, M.; Mourad, M. C. D.; Vroon, Z. Antireflective Coatings for Glass and Transparent Polymers. *Langmuir* **2016**, *32*, 6781−6793.
(34) Zhang, C.; Zhao, H.; Su, Y.; Wang, H.; Shen, J.; Wang, X. Embedding Constructed Refractive Index Graded Antireflective Coating with High Abrasion Resistance and Environmental Stability for Polycarbonate Glass. *J. Colloid Interface Sci.* **2022**, *608*, 13−21.

https://doi.org/10.1021/acsami.3c17986
ACS Appl. Mater. Interfaces 2024, 16, 10714−10721

(35) Lee, G.; Kim, M.-C.; Choi, Y. W.; Ahn, N.; Jang, J.; Yoon, J.; Kim, S. M.; Lee, J.-G.; Kang, D.; Jung, H. S.; et al. Ultra-Flexible Perovskite Solar Cells with Crumpling Durability: Toward a Wearable Power Source. *Energy Environ. Sci.* **2019**, *12*, 3182−3191.
(36) Wan, Y.; Yu, S.-H. Polyelectrolyte Controlled Large-Scale Synthesis of Hollow Silica Spheres with Tunable Sizes and Wall Thicknesses. *J. Phys. Chem. C* **2008**, *112*, 3641−3647.
(37) Tan, G.; Lee, J. H.; Lan, Y. H.; Wei, M. K.; Peng, L. H.; Cheng, I. C.; Wu, S. T. Broadband Antireflection Film with Moth-Eye-Like Structure for Flexible Display Applications. *Optica* **2017**, *4*, 678−683.
(38) Sheldon, B.; Haggerty, J. S.; Emslie, A. G. Exact Computation of the Reflectance of a Surface Layer of Arbitrary Refractive-Index Profile and an Approximate Solution of the Inverse Problem. *J. Opt. Soc. Am.* **1982**, *72*, 1049−1055.
(39) Jia, G.; Ji, Z.; Wang, H.; Chen, R. Preparation and Properties of Five-Layer Graded-Refractive-Index Antireflection Coating Nanostructured by Solid and Hollow Silica Particles. *Thin Solid Films* **2017**, *642*, 174−181.

https://doi.org/10.1021/acsami.3c17986
ACS Appl. Mater. Interfaces 2024, 16, 10714−10721